Insights into palladium poisoning of Cu/SSZ-13 selective catalytic reduction catalysts

Yiqing Wu [a], Yilin Wang [a], Eric D. Walter [a], Kenneth G. Rappé [a], Yong Wang [a,b], Feng Gao [a,*]

[a] *Institute for Integrated Catalysis, Pacific Northwest National Laboratory, P.O. Box 999, Richland, WA 99354, USA*
[b] *Voiland School of Chemical Engineering and Bioengineering, Washington State University, Pullman, WA 99163, USA*

ARTICLE INFO

ABSTRACT

The impacts of Pd poisoning to the activity, selectivity, and hydrothermal stability of Cu/SSZ-13 selective catalytic reduction (SCR) catalysts are reported. Pd lowers DeNOx efficiency of Cu/SSZ-13 via two mechanisms: (1) displacing SCR active sites in the form of isolated Pd-ions, and (2) catalyzing non-selective NH_3 oxidation in the form of PdO. The first mechanism works by the diffusion of isolated Pd-ions into chabazite cages to displace $ZCu^{II}OH$ SCR active species, and it occurs on Cu/SSZ-13 catalysts with and without external surface CuO clusters in similar fashion. In contrast, the second mechanism works differently with and without external surface CuO clusters. For Cu/SSZ-13 catalyst without external CuO clusters (i.e., primarily isolated Cu-ions), PdO leads to significant decrease of DeNOx efficiency at reaction temperatures above ~400 °C due to its non-selective NH_3 oxidation activity at high temperatures. However, this poisoning effect becomes much less impactful on Cu/SSZ-13 catalyst containing CuO clusters. This is due to the formation of CuO-PdO solid solution via interactions between CuO and PdO, which reduces non-selective NH_3 oxidation potential. Furthermore, this solid solution formation even mitigates adverse effects caused by hydrothermal aging. Hence, the poisoning effects of Pd are closely related to Cu speciation and spatial distribution of a Cu/SSZ-13 catalyst. Finally, this study suggests a strategy in eliminating Pd poisoning, that is, the introduction of an oxide phase that effectively traps PdO but does not adversely influence SCR.

1. Introduction

Selective catalytic reduction (SCR) of NOx by ammonia has achieved great success in commercial applications, with wide implementation of Cu-exchanged SSZ-13 zeolite catalysts as the core NOx-reduction component of emission control systems for diesel vehicles and trucks [1–3]. In heavy-duty vehicle aftertreatment systems, diesel oxidation catalyst (DOC) and diesel particulate filter (DPF) are typically employed upstream of the SCR unit to oxidize unburned hydrocarbons and CO in the exhaust gas, and to filter & manage diesel particulate and soot, respectively [3]. In recent years, passive NOx adsorber (PNA) has also been investigated to tackle "cold start" NOx emissions by adsorbing NOx at low temperatures and releasing it after the downstream SCR system reaches operational temperatures [4–6]. Although the integration of DOC, PNA, DPF and SCR is key to meeting the increasingly stringent emission regulations [3], the volatilization of PGMs in DOC, PNA and DPF units (e.g., during DPF regeneration or desulfation events) poses a practical threat to proper downstream SCR function. This is because

PGMs strongly catalyze the oxidation of NH_3 to NOx; their deposition on the SCR unit can deplete NH_3 availability and lower DeNOx efficacy [7]. Moreover, SCR applications typically use enhanced urea injection to maximize NOx conversion. This practice generates unwanted "ammonia slip", which requires ammonia oxidation (AMOX) catalysts, also called ammonia slip catalysts (ASC), positioned downstream of the SCR unit to eliminate the adverse environmental impacts of ammonia slip. State-of-the-art ASCs adopt a layered structure where a Cu/SSZ-13 catalyst layer is underneath an alumina supported PGM catalyst layer, on which a portion of the NH_3 slipped from SCR is oxidized by the PGM layer to NOx, followed by its reaction to the remaining slipped NH_3 via SCR in the Cu/SSZ-13 layer [8–10]. This catalyst fabrication approach can also lead to PGM penetration into the Cu/SSZ-13 catalyst layer during high-temperature treatments.

Because of the reasons described above, the impacts of PGM poisoning to SCR catalyst have attracted increasing attention in recent years. Leistner et al. studied volatilization of Pt on a wash-coated model SCR catalyst and found that its volatilization increased exponentially

---

* Corresponding author.
  E-mail address: feng.gao@pnnl.gov (F. Gao).

with temperature and the deposited PtO_x strongly promoted the unwanted NH_3 oxidation reaction within the SCR unit [7]. Lezcano-Gonzalez et al. reported that the deposition of PGMs on the SCR unit led to a considerable increase in the selectivity to N_2O and NO_2 but showed less impacts on the SCR active sites or the structure of the zeolite support [11]. Regarding dual-layer ASC, severe poisoning effects of PGMs were also reported, which led to undesirable high selectivity of NO_x [8,10]. In addition to adverse effects, a study by Yu et al. demonstrated that Pt species reacted with CuO clusters to form copper-platinum oxo-complexes and thus increased the hydrothermal stability of Cu/SAPO-34 SCR catalysts [12].

Given its wide use and high volatility at high temperatures, Pt poisoning is more frequently found than that from other PGMs. As such, most of the prior studies focused on poisoning effects of Pt. However, Pd is also commonly used in DOC, PNA and ASC, justifying the importance of studying the negative impacts of Pd to SCR catalysts. Herein we aim to reveal the detailed impacts of Pd on the activity, selectivity, and hydrothermal stability of Cu/SSZ-13 SCR catalyst. Hence, we synthesized two Pd-Cu/SSZ-13 catalysts with different Cu speciation and carried out hydrothermal aging treatments to evaluate their hydrothermal stability. The morphology, composition and active site distribution of these samples were characterized and their performance in SCR and NH_3 oxidation reactions were evaluated. We discovered that the impacts of Pd addition are closely related to Cu speciation and spatial distribution for both fresh and hydrothermally aged Cu/SSZ-13 samples. These findings shed lights on rational designing of diesel engine exhaust aftertreatment systems.

2. Experiments

2.1. Catalyst synthesis

Na/SSZ-13 zeolite (Si/Al ratio = 12) was hydrothermally synthesized in house. In a typical synthesis, 0.8 g of NaOH (Sigma Aldrich, >99%) was dissolved in 38 ml of deionized (DI) water followed by addition of 17 g of TMAda-OH (Sachem Inc., 25% N,N,N-trimethyl-1-adamantyl ammonium hydroxide) as the structure-directing agent (SDA) and 1.5 g of $Al(OH)_3$ (Sigma Aldrich, ~54% Al_2O_3) under continuous stirring. Upon homogenization, 40.0 g of LUDOX AS-30 colloidal silica (Sigma Aldrich, 30 wt% suspension in H_2O) was added slowly to the solution until a uniform white gel was formed. The gel was sealed in a 125-ml Teflon-lined stainless-steel autoclave containing a magnetic stir bar which was placed in a sand bath on top of a hot plate stirrer. Hydrothermal synthesis was carried out at 160 °C under continuous stirring at 400 rpm for 4 days. After synthesis, the solid sample was collected by centrifugation, washed three times with deionized water, dried under a N_2 flow at 70 °C overnight and calcined in static air at 650 °C for 5 h to burn off the SDA. The as-prepared Na/SSZ-13 was then converted to NH_4/SSZ-13 by ion-exchanging twice with 0.1 M NH_4NO_3 solution at 80 °C for 2 h and drying under a N_2 flow at 70 °C overnight.

Two Cu/SSZ-13 catalysts were synthesized for this study. In the first synthesis, 5 g of NH_4/SSZ-13 was dispersed in a 500 ml aqueous solution of 0.01 M $Cu(NO_3)_2$ (Sigma Aldrich, >99.0%) under stirring at 300 rpm. The ion-exchange was carried out at 80 °C for 2 h under stirring, and the resulting solid was recovered via centrifugation and washed twice with deionized water. The ion-exchange process was repeated one additional time to improve Cu exchange level. Again, after centrifugation and washing with deionized water, the solid was dried at 70 °C in a N_2 flow. The Cu content of this sample was 1.95 wt% as determined via inductively coupled plasma atomic emission spectroscopy (ICP-AES) at Galbraith Laboratories (Knoxville, TN, United States). In the following, this sample is denoted "2Cu". In the second synthesis, 3 g of NH_4/SSZ-13 was first dispersed in 100 ml of deionized water under stirring at 300 rpm followed by addition of 0.31 g of $Cu(NO_3)_2 \bullet 2.5 H_2O$ (Sigma Aldrich, >99.0%). The ion exchange was carried out at 80 °C for 2 h under

stirring. After that, the temperature was raised to 100 °C to evaporate water and recover the dry powder. This sample contains 2.84% Cu determined via ICP-AES and is thus denoted "3Cu" in the following. After synthesis, both samples were calcined in static air at 550 °C for 5 h and then stored at ambient conditions as our fresh catalysts.

~1 wt% Pd was loaded onto the 2Cu and 3Cu samples via incipient wetness impregnation, using tetraamine palladium(II) nitrate aqueous solution (10 wt% Pd, Sigma Aldrich) as the Pd precursor. After drying in flowing N_2 at 70 °C, the samples were calcined in static air at 550 °C for 5 h. ICP-AES analysis demonstrated that Pd loadings of the 2Cu and 3Cu samples are 0.81% and 0.88%, respectively. In the following, these two Pd-Cu/SSZ-13 catalysts are denoted "2Cu1Pd" and "3Cu1Pd". For comparison, a Pd/SSZ-13 sample with ~1 wt% Pd loading was also prepared via impregnating the same Pd precursor on NH_4/SSZ-13, followed by the same drying and calcination treatments. This latter sample is denoted "1 Pd" in the following.

To study hydrothermal stability of these catalysts, a portion of the fresh samples was subjected to hydrothermal aging in 10% H_2O/air flow at 800 °C for 24 h. The hydrothermally aged catalysts are designated with "-HTA" in the following. For example, "2Cu1Pd-HTA" denotes the hydrothermally aged 2Cu1Pd catalyst.

2.2. Characterization

Cu and Pd loadings were determined by ICP-AES as described above. Brunauer–Emmett–Teller (BET) surface areas and micropore volumes of the catalysts were measured on a Quantachrome Autosorb-IQ3 analyzer with liquid N_2 adsorption. The catalysts were degassed under vacuum overnight at 300 °C prior to analysis. Powder X-ray diffraction (XRD) measurements were performed on a Shimadzu powder X-ray diffractometer with CuKa radiation (k = 1.5406 Å). The morphology of the catalysts was probed with transmission electron microscopy (TEM) on a spherical aberration-corrected FEI Titan 300 kV 80–300 microscope.

Note that the ways we used to prepare the two Cu/SSZ-13 catalysts lead to a difference in Cu speciation and distribution. The 2Cu sample was prepared by standard solution ion-exchange; as such, it is anticipated that isolated Cu^{II}-ions dominate. The 3Cu sample, on the other hand, involved slurry drying. Therefore, unexchanged $Cu(NO_3)_2$ in the slurry is anticipated to deposit on zeolite external surfaces during drying and then convert to CuO clusters during the subsequent calcination. As such, isolated Cu^{II}-ions and CuO clusters are anticipated to coexist on 3Cu.

Two methods were applied for revealing Cu speciation and distribution: electron paramagnetic resonance (EPR) spectroscopy and H_2 temperature-programmed reduction (H_2-TPR). Isolated Cu^{II}-ions in the samples were quantified by EPR spectroscopy [13]. Measurements were carried out on a Bruker E580 X-band spectrometer in continuous wave mode, with the magnetic field sweeping between 2400 and 3600 G in 83 s with a time constant of 83 ms. The field was modulated at 100 kHz and with an amplitude of 5 G, and the microwave frequency was set at 9.3 GHz with a power of 0.2 mW. Typically, 30 mg of ambient hydrated catalyst was loaded into a quartz EPR tube, and continuous scans were performed after cooling the sample to − 150 °C with liquid N_2 to immobilize Cu^{II}-ions. The acquired spectra were double-integrated to obtain signal peak areas, which are proportional to EPR-active isolated Cu(II) content. Quantification was achieved using a linear calibration curve obtained from a series of standard solutions with different isolated Cu^{II}-ion concentrations that were prepared by dissolving $Cu(NO_3)_2 \bullet 2.5 H_2O$ and imidazole (Sigma Aldrich, 99.0%) in ethylene glycol (Sigma Aldrich, 99.8%). Imidazole was used here to coordinate with Cu(II) ions to prevent formation of EPR-silent multinuclear Cu species. To distinguish various isolated Cu^{II}-ions, measurements were also carried out on dehydrated catalysts. Sample dehydration was achieved by flowing dry N_2 through the samples at 250 °C for 60 min; measurements were done after cooling the samples back to − 150 °C.

H_2-TPR experiments were conducted on a Micromeritics AutoChem

2920 apparatus. Typically, 100 mg of sample was first purged with He at room temperature for ~30 min. After that, 10% H_2/Ar was introduced at a flow rate of 50 ml/min. The catalyst was then ramped from ambient to 1050 °C at 10 °C/min and maintained at 1050 °C for 15 min before cooling. H_2 consumption was quantified using TPR of a reference sample (Ag_2O, provided by Micromeritics) under the same condition. NH_3 temperature-programmed desorption (NH_3-TPD) was carried out on the same apparatus coupled with a MKS Cirrus 2 mass spectrometer. Typically, 100 mg of sample was first treated under a He flow of 50 ml/min at 550 °C for 1 h. The sample was then cooled to 110 °C at which, NH_3 adsorption was carried out under a 1% NH_3/He flow of 50 ml/min until saturation (i.e., outlet NH_3 concentration became invariant with time). Weakly adsorbed NH_3 was then removed by purging under a 50 ml/min He flow for 1 h. NH_3-TPD was then carried out by ramping the sample to 800 °C at 10 °C /min with NH_3 desorption monitored with the mass spectrometer.

2.3. Catalytic performance

Standard NH_3-SCR ($4NO + 4NH_3 + O_2 = 4 N_2 + 6 H_2O$) "light-off" tests were conducted on a custom-built plug-flow SCR reaction test stand equipped with an online MKS MultiGas 2030 FTIR gas analyzer with the gas cell retained at 191 °C for measuring concentrations of the reactants and products. A mass of 30 mg of sieved catalyst (60–80 mesh) was supported on a quartz frit inside a 0.8-cm inner diameter quartz reactor placed in an electric tube furnace. The composition of the gas feed was 350 ppm NH_3, 350 ppm NOx (NO dominant, containing ~10 ppm NO_2), 14% O_2, 2.5% H_2O, and balance N_2. The total flow rate was 225 ml/min, and the gas hourly space velocity (GHSV) was estimated to be 300,000 h^{-1}. Measurements were conducted at temperatures decreasing stepwise from 550° to 100°C with intervals of 50 or 20 °C. Reaction at each temperature was maintained for at least 45 mins to reach steady state. NH_3 oxidation tests ($4NH_3 + 3 O_2 = 2 N_2 + 6 H_2O$) were carried out in the same manner.

NOx and NH_3 conversions were calculated using the following equations:

$$NOx \ conversion = \frac{(NOx)_{inlet} - (NOx)_{outlet}}{(NOx)_{inlet}} \times 100\%$$

$$NH_3 \ conversion = \frac{(NH_3)_{inlet} - (NH_3)_{outlet}}{(NH_3)_{inlet}} \times 100\%$$

3. Result and discussion

3.1. Characterizations

3.1.1. Textural properties

Table 1 presents the results of surface area (SA) and pore volume

Table 1
Surface area and pore volume values of the parent SSZ-13 support, and fresh and hydrothermally aged Cu/SSZ-13 and Pd-Cu/SSZ-13 samples, determined by liquid N_2 adsorption.

Sample	S_{total}^a (m²/g)	S_{micro}^b (m²/g)	V_{total}^c (cm³/g)	V_{micro}^b (cm³/g)
Parent SSZ-13	790	679	0.356	0.254
2Cu	761	673	0.341	0.252
2Cu1Pd	662	587	0.302	0.22
3Cu	720	637	0.318	0.238
3Cu1Pd	730	644	0.326	0.242
2Cu-HTA	729	652	0.327	0.245
2Cu1Pd-HTA	712	630	0.324	0.236
3Cu-HTA	686	614	0.305	0.23
3Cu1Pd-HTA	664	519	0.337	0.199

Note: [a]determined using multi-point BET method; [b] calculated using t-plot method; [c] obtained at $P/P_0 = 0.95$.

(PV) analyses of the fresh and hydrothermally aged Cu-Pd/SSZ-13 catalysts. For comparison, SA and PV values from the parent SSZ-13 support are also included. Fresh 2Cu and 3Cu samples show small decreases in their SA/PV versus the SSZ-13 support; this is likely the result of minor support degradation during ion exchange. The decreases are slightly more severe for 3Cu versus 2Cu, and therefore another possible contributor is the deposition of CuO clusters clogging support pores/channels. Upon Pd deposition, however, these two samples show clear differences. The 3Cu and 3Cu1Pd samples display essentially identical SA/PV, whereas 2Cu1Pd shows marked losses as compared to 2Cu. This suggests that Pd deposited on 2Cu clogs support pores/channels more severely. Upon hydrothermal aging, 2Cu, 3Cu and 3Cu1Pd samples display small SA/PV losses as compared to their fresh counterparts. This is fully anticipated: hydrothermal aging under such a harsh condition typically causes degradation of SSZ-13 support. However, the 2Cu1Pd-H sample displays increase of SA/PV as compared to fresh 2Cu1Pd. This strongly suggests that the abnormally low SA/PV of fresh 2Cu1Pd is due to Pd clogging, and aging appears to alleviate this effect.

XRD measurements were conducted to gain additional insights into the textural properties of the catalysts, and the results are shown in Fig. 1. Fresh samples (Fig. 1a) display solely chabazite diffraction patterns of the SSZ-13 support. The absence of CuO (expected at 35.4°,
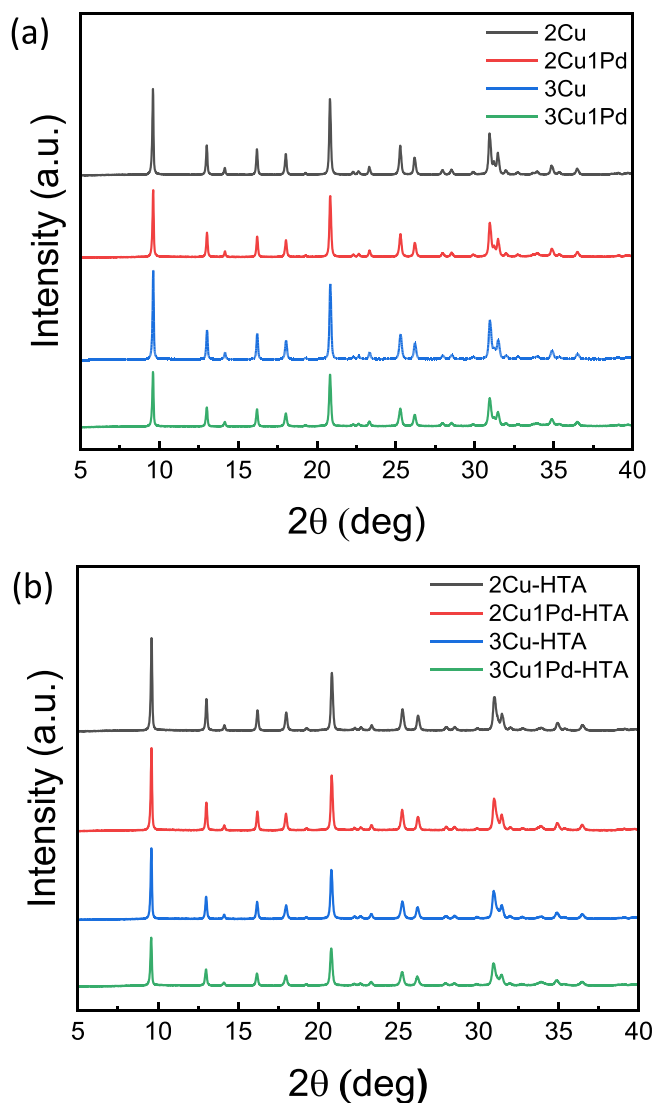

(a)

(b)

Fig. 1. XRD patterns for (a) fresh, and (b) hydrothermally aged Cu/SSZ-13 and Cu-Pd/SSZ-13 catalysts.

38.0°) [9,14] and PdO (expected at 34.1°, 42.2°) [15,16] diffractions suggests that either these species are not present or their presence and/or morphology are below the detection limit. Their presence will be confirmed with more sensitive characterizations below. As Fig. 1b shows, the hydrothermally aged samples display similar XRD patterns as their respective fresh samples; this indicates the absence of severe structural damages or evident aggregations of Cu and Pd species during the harsh hydrothermal aging process, which is consistent with Table 1.

3.1.2. Quantification of Cu species

Literature clearly documents that Cu/SSZ-13 contains two SCR-active isolated Cu^{II} species: Z_2Cu^{II} and $ZCu^{II}OH$ ions [17–20]. CuO clusters are also commonly present in catalysts prepared with certain methods (e.g., impregnation followed by calcination), with Cu loadings beyond ion-exchange capacities, or after hydrothermal aging treatments [21,22]. In the following, we applied H_2-TPR and EPR to quantify the various Cu moieties.

Fig. 2 presents H_2-TPR profiles of the fresh 2Cu and 3Cu samples. Measurements were carried out on ambient hydrated samples to avoid possible auto-reduction of Cu^{II}-ions to Cu^I-ions that can occur during dehydration in inert atmospheres [23,24]. The 2Cu sample displays reduction events at two temperatures: a low-temperature reduction centered at ~220 °C with a high-temperature shoulder extending to ~400 °C, and a high-temperature reduction centered ~1000 °C. Based on literature assignments, the 220 °C reduction event is $ZCu^{II}OH$ reduction to ZCu^I with the shoulder primarily due to Z_2Cu^{II} reduction to ZCu^I, and the high-temperature peak is due to reduction of ZCu^I to Cu^0 [25–27]. Peak area analysis reveals essentially identical H_2 consumption during the low- and high-temperature reduction events. Note that CuO clusters reduce to Cu^0 around ~300 °C, and thus their presence only contributes to H_2 consumption at low-temperatures [26]. As such, the peak area analysis result suggests the absence of CuO in our 2Cu sample. Peak area analysis also reveals an isolated Cu content of ~2.04%, consistent with the total Cu content of 1.95% as determined via ICP-AES.

The fresh 3Cu sample displays reduction peaks occurring at similar temperatures as those of 2Cu as well as additional weak H_2 consumption at ~500 and ~750 °C. This additional H_2 consumption is attributed to reduction of less stable isolated Cu^I-ions (ZCu^I). By integrating peak areas below and above ~400 °C, it is revealed that H_2 consumption below 400 °C is considerably larger than that above 400 °C. Based on discussions above, this finding confirms the presence of CuO clusters in our fresh 3Cu sample [26]. Via peak area analysis, we estimate that the 3Cu sample contains ~80% (2.27%) isolated Cu-ions and ~20% (0.57%) CuO clusters.
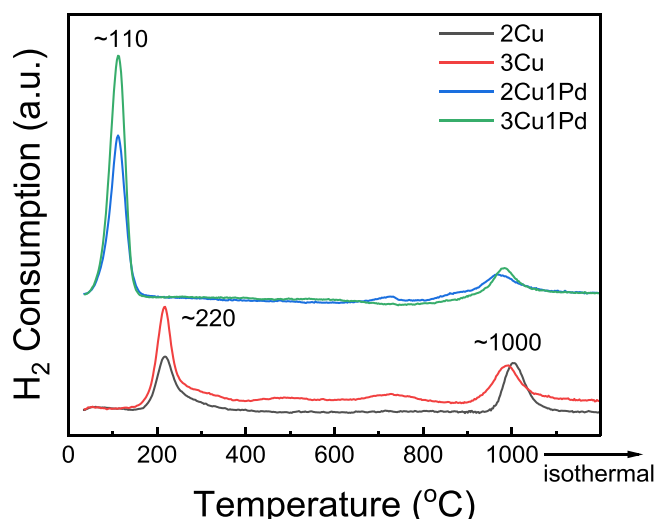
H_2-TPR profiles for the fresh 2Cu1Pd and 3Cu1Pd samples are also displayed in Fig. 2. Again, since ambient hydrated samples are used, both Cu and Pd are in their + 2 oxidation states prior to measurements. The low temperature reduction event is shifted to ~110 °C, and it occurs with much higher peak intensities versus the respective Cu/SSZ-13 samples. Therefore, in addition to isolated Cu^{II}-ions and CuO clusters, reduction of Pd species (e.g., isolated Pd-ions, PdO clusters and particles) to Pd^0 also contributes at low-temperatures. Since Pd^0 is known to readily activate H_2, the reduction temperature shift from ~220 °C to ~110 °C for isolated Cu^{II}-ions can be explained via a hydrogen spillover effect from Pd as suggested in previous studies [28,29]. Based on H_2-TPR measurements of a series of reference Pd/SSZ-13 samples (Fig. S1), we also cannot rule out the formation of Pd-hydride species in the low-temperature regime of our TPR process [30]. Both 2Cu1Pd and 3Cu1Pd samples display similar high temperature reduction peaks around 1000 °C as their Pd-free counterparts but with substantial losses in intensity. In addition, 2Cu1Pd also displays a weak reduction peak ~730 °C attributed to less stable ZCu^I. Note that the 2Cu sample does not display this reduction state. These latter observations suggest either that the introduction of Pd destabilizes a portion of Cu^{II}-ions in 2Cu and 3Cu, or that the same hydrogen spillover effect renders reduction of ZCu^I more readily. Overall, the introduction of Pd markedly alters both low- and high-temperature reduction behavior of the 2Cu1Pd and 3Cu1Pd samples and makes quantification of isolated Cu^{II}-ions and CuO clusters difficult. We also carried out H_2-TPR measurements of the hydrothermally aged catalysts. However, the H_2-TPR profiles become much less resolved, preventing the derivation of useful information for this study; as such, the results are not presented here.

Next, EPR was applied for more detailed Cu speciation and quantification. EPR has been widely used to study isolated Cu^{II}-ions in Cu/zeolites due to its quantitative nature and excellent resolution [17,31,32]. Owing to the presence of unpaired electrons, isolated Cu^{II}-ions are EPR active. In contrast, isolated Cu^I-ions and CuO clusters are EPR silent because of the lack of unpaired electrons and antiferromagnetic effects, respectively. Regarding Z_2Cu^{II} and $ZCu^{II}OH$ sites in Cu/SSZ-13, previous studies revealed that both are EPR active when they are solvated by H_2O molecules [17,26]. Upon dehydration, study by Mossin and coworkers demonstrated that Z_2Cu^{II} remains EPR active due to its square planar Cu-O coordination; conversely, the 3 Cu-O coordinated $ZCu^{II}OH$ becomes EPR silent due to a pseudo Jahn–Teller effect [33]. It is interesting to note that during sample dehydration, $ZCu^{II}OH$ can undergo additional chemistry depending on whether dehydration is carried out in an inert atmosphere or in O_2. In an inert atmosphere, a portion of $ZCu^{II}OH$ can undergo autoreduction to ZCu^I [34]; in O_2, $ZCu^{II}OH$ can dimerize to Cu^{II}-O_2-Cu^{II} moieties [35]. Both ZCu^I and Cu^{II}-O_2-Cu^{II} are EPR silent. As such, Z_2Cu^{II} and $ZCu^{II}OH$ should in principle be readily distinguished and quantified by EPR measurements of both hydrated and dehydrated samples. A more recent study by Chiesa and coworkers [36], however, demonstrated that some (but not all) $ZCu^{II}OH$ remains EPR active upon sample dehydration, making quantification more complicated. Fig. 3 (a)–(d) presents EPR spectra for hydrated and dehydrated fresh and HTA samples. Note that for each series of measurements, spectra lineshapes are essentially identical suggesting that the presence of Pd induces no or undetectable changes to structure and bonding of the remaining isolated Cu^{II}-ions. As shown in Fig. 3(a), hydrated fresh catalysts display essentially identical spectrum lineshapes and common spin-Hamiltonian parameters $g_{||} = 2.399$ and $A_{||} = 134$ G. Such similarity is anticipated since fully and partially solvated Cu^{II}-ions adopt highly similar Cu-O coordinations. Fig. 3(b) depicts spectra for the dehydrated fresh catalysts. Each sample now displays two sets of hyperfine features. Signals at $g_{||} = 2.365$ and $A_{||} = 140$ G are due to Z_2Cu^{II}, and signals at $g_{||} = 2.314$ and $A_{||} = 114$ G are due to $ZCu^{II}OH$ according to Chiesa and coworkers [36]. Fig. 3(c) presents spectra for the hydrated HTA samples. Again, since all hydrated Cu^{II}-ions adopt highly similar Cu-O coordination environments, they display identical $g_{||}$ and $A_{||}$ tensor values. Finally, Fig. 3(d) depicts spectra for the dehydrated HTA samples. It is important
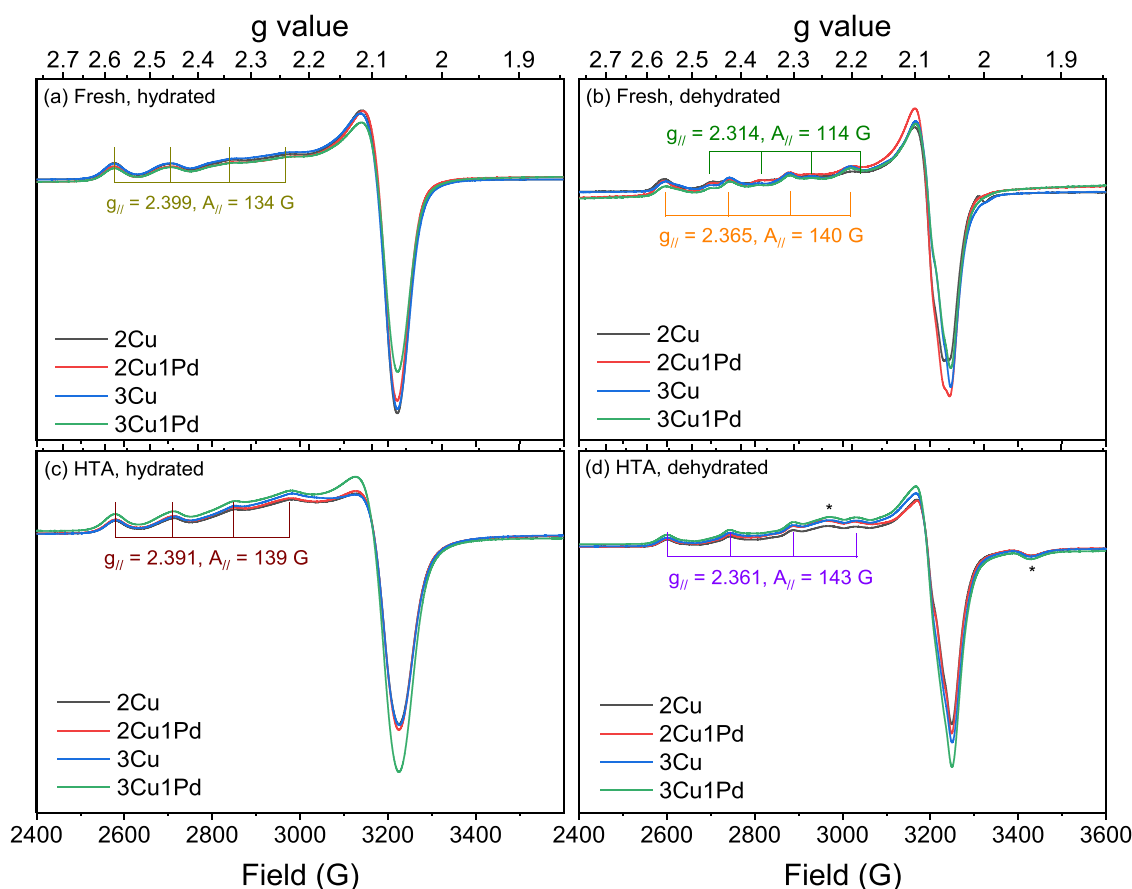

Fig. 2. H_2-TPR profiles for the fresh Cu/SSZ-13 and Pd-Cu/SSZ-13 catalysts.

Fig. 3. EPR spectra for Cu/SSZ-13 and Cu-Pd/SSZ-13 samples. (a) fresh, hydrated; (b) fresh, dehydrated; (c) HTA, hydrated; (d) HTA, dehydrated.

to note that ZCu^{II}OH signals are now barely detectable, consistent with the fact that ZCu^{II}OH converts to more stable Cu moieties during hydrothermal aging [37,38]. The dehydrated HTA samples also display new features marked with asterisks (*). These signals appear due to coupling between isolated Z$_2$Cu^{II} sites that display exceedingly small EPR interspin distances of ~3.9 Å [39].

Based on the spectra shown in Fig. 3, Z$_2$Cu^{II} and ZCu^{II}OH quantification of the HTA samples is straightforward, where EPR areas of the dehydrated samples are due to Z$_2$Cu^{II}, and EPR area differences between hydrated and dehydrated samples are due to ZCu^{II}OH. For the fresh samples, since some ZCu^{II}OH is still detected in dehydrated samples, additional spectra simulations were carried out to derive ZCu^{II}OH/ Z$_2$Cu^{II} ratios of EPR active Cu, detailed in Fig. S2 and Table S1 of the Supplementary Material. In this case, two pieces of information are needed for ZCu^{II}OH quantification in fresh catalysts: (1) EPR area differences between hydrated and dehydrated samples, and (2) ZCu^{II}OH/ Z$_2$Cu^{II} ratios of EPR active Cu in dehydrated samples. The results are tabulated in Table 2. A few points are worth noting regarding these data:

1. For both fresh 2Cu and 3Cu samples, isolated Cu^{II} quantification via EPR matches well with that via H$_2$-TPR. Both measurements reveal a key difference between these two samples, i.e., small amount of CuO (0.6–0.7 wt%) is present in the 3Cu sample, but its content on 2Cu is negligible.
2. Hydrothermal aging of the 2Cu and 3Cu samples causes substantial transformation of ZCu^{II}OH to Z$_2$Cu^{II}. According to previous studies [31,40], this is due to the following reaction: ZCu^{II}OH + ZH → Z$_2$Cu^{II} + H$_2$O. Both samples also show minor losses of total isolated Cu-ions, due likely to Cu agglomeration.
3. Upon Pd deposition on fresh 2Cu and 3Cu, isolated Cu^{II} contents also decrease, with extents similar to those caused by hydrothermal aging. As such, the decrease of high-temperature Cu^I reduction over the Pd-loaded samples found in H$_2$-TPR (Fig. 2) is due more to loss of isolated Cu^{II}-ions than to a hydrogen spillover effect. It is important to note that the isolated Cu^{II} content decrease upon Pd deposition is due primarily to ZCu^{II}OH loss; Z$_2$Cu^{II} contents remain largely invariant before and after Pd deposition. Such a result can only be rationalized by invoking the diffusion of Pd-ions into chabazite pores and likely occurs during catalyst calcination. These Pd-ions then compete with ZCu^{II}OH for extraframework exchange positions, forcing some of the latter species to agglomerate to EPR silent Cu moieties.
4. Hydrothermal aging of the 2Cu1Pd and 3Cu1Pd samples also causes substantial transformation of ZCu^{II}OH to Z$_2$Cu^{II}. However, a major difference between the samples is that hydrothermal aging decreases the total isolated Cu^{II} content of 2Cu1Pd but increases the total isolated Cu^{II} content of 3Cu1Pd suggesting CuO redispersion during aging.

Table 2
Isolated Cu^{II}-ion contents of the fresh and hydrothermally aged Cu/SSZ-13 and Pd-Cu/SSZ-13 samples, determined by EPR.

Sample	Total isolated Cu^{II}-ions (wt%)	Z$_2$Cu^{II} (wt%)	ZCu^{II}OH (wt%)
2Cu	1.92	0.39	1.53
2Cu1Pd	1.67	0.50	1.17
3Cu	2.08	0.48	1.60
3Cu1Pd	1.67	0.46	1.21
2Cu-HTA	1.66	1.29	0.37
2Cu1Pd-HTA	1.60	1.16	0.43
3Cu-HTA	1.63	1.41	0.22
3Cu1Pd-HTA	1.98	1.58	0.40

3.1.3. Pd speciation and distribution

As discussed immediately above, our EPR quantification results shown in Table 2 suggest that some Pd in the 2Cu1Pd and 3Cu1Pd samples migrates into the chabazite pores as Pd-ions, which destabilizes $ZCu^{II}OH$. To further confirm this notion, we carried out NH$_3$-TPD. As shown in Fig. 4, 2Cu and 3Cu samples display three NH$_3$ desorption peaks centered at ~191, 311 and 475 °C, respectively. Based on literature assignments, these are assigned to NH$_3$ desorbing from weak acid sites (e.g., extraframework Al), Cu-ions, and Brønsted acid sites, respectively [9,24]. Upon Pd deposition, at least two changes are worth noting:

1. 2Cu1Pd and 3Cu1Pd display clear decreases in their 475 °C peaks versus 2Cu and 3Cu consistent with the formation of Pd-ions that replace charge-balancing protons.
2. 2Cu1Pd and 3Cu1Pd also display clear decreases in their 311 °C peaks consistent with $ZCu^{II}OH$ loss (Table 2).

Interestingly, 2Cu1Pd and 3Cu1Pd display a new NH$_3$ desorption peak at ~266 °C that can be attributed to Pd-ions. Therefore, the presence of atomically dispersed Pd-ions in zeolite exchange positions can be unambiguously confirmed based on corroborating EPR and NH$_3$-TPD results. Unfortunately, quantification of such species cannot be achieved based on the catalyst characterizations shown here. We also attempted to identify possible nature of the Pd-ions in 2Cu1Pd and 3Cu1Pd via NO adsorption IR measurements; NO adsorption has been frequently used in the past to probe Cu- and Pd-ions [15,41,42]. Unfortunately, these two moieties cannot be distinguished by NO vibrations. Still, analogous to Cu^{II}-ions in Cu/SSZ-13, it can be postulated that Pd-ions are stabilized by chabazite framework single, or pair charges as $ZPd^{II}OH$, or Z_2Pd^{II}, respectively. Note that in recent Pd/SSZ-13 PNA studies, both species have been proposed [15,41]. Based on Z_2Cu^{II} and $ZCu^{II}OH$ quantification data shown in Table 2, it can be further postulated that Z_2Pd^{II} is thermodynamically less stable than Z_2Cu^{II} and is thus unable to destabilize the latter. On the other hand, $ZPd^{II}OH$ appears to have comparable stability to $ZCu^{II}OH$ which leads to partial displacement of the latter.

Since our 2Cu and 3Cu samples are already rather heavily loaded with Cu, it is unlikely that all Pd deposited on 2Cu1Pd and 3Cu1Pd diffuses into zeolite pores and resides stably atomically dispersed. Thus, we applied TEM imaging to probe external surface Pd moieties. Fig. 5 presents TEM images for the 2Cu, 3Cu, 2Cu1Pd and 3Cu1Pd samples. No CuO particles are observed on 2Cu or 3Cu samples. This result is anticipated for 2Cu since this sample predominately contains atomically dispersed Cu-ions. For the 3Cu sample, since both H$_2$-TPR and EPR measurements confirm the presence of ~20% Cu as CuO clusters, they

must be highly dispersed and thus too small to be observed by our TEM. As such, the precise locations of these clusters are not clear, i.e., whether these are located inside chabazite pores or on external surfaces. Uniformly dispersed particles measuring 2–6 nm are observed in TEM imaging on the 2Cu1Pd and 3Cu1Pd samples; these are attributed to external surface PdO particles. Their presence is in accordance with the sharp H$_2$ consumption peaks at ~110 °C shown in Fig. 2. Even though the PdO particles on the two samples do not appear to differ appreciably via TEM, we believe that there exists a major difference in external surface Pd deposition on these two samples. Recalling the data shown in Table 1, the surface area of 2Cu1Pd is ~100 m^2/g lower than that of 2Cu, whereas surface area of 3Cu1Pd is even slightly higher than that of 3Cu. To explain this difference, we hypothesize that PdO nucleation occurs at chabazite pore openings on 2Cu, leading to clogging of a portion of pores/channels; in contrast, PdO nucleation occurs at external surface CuO clusters on 3Cu, precluding additional clogging effects. For this hypothesis to apply, the presence of external surface CuO on the 3Cu sample is a prerequisite. Even though this cannot be confirmed via TEM (Fig. 5), the way that we prepared the 3Cu sample is in line with the presence of external surface CuO: upon slurry drying, the unexchanged Cu(NO$_3$)$_2$ must deposit on the support external surface. The subsequent calcination temperature at 550 °C is sufficiently high to decompose Cu(NO$_3$)$_2$, but not high enough to drive excessive Cu diffusion into zeolite pores [43]. In the presence of external surface CuO clusters, PdO nucleation onto which is due to strong affinity between PdO and CuO, as reported previously [44,45].

3.2. SCR and NH$_3$ oxidation reactions

To reveal Pd poisoning mechanisms, standard SCR (4NO + 4NH$_3$ + O$_2$ = 4 N$_2$ + 6 H$_2$O) and NH$_3$ oxidation (4NH$_3$ + 3 O$_2$ = 2 N$_2$ + 6 H$_2$O) reactions were carried out on both fresh and hydrothermally aged catalysts to evaluate the impacts of Pd on catalyst activity, selectivity and stability. All measurements were conducted under steady-state conditions.

3.2.1. Fresh catalysts

Fig. 6 shows the SCR activity plots versus temperature over the fresh Cu/SSZ-13 and Cu-Pd/SSZ-13 samples; Fig. 6a presents NOx conversion results and Fig. 6b presents NH$_3$ conversion results. For comparison and completeness, reaction data over the 1 Pd reference sample are also included in these plots. To facilitate discussions below, we divide these reaction data into three temperature regimes: low temperatures (100–200 °C), intermediate temperatures (200–400 °C), and high temperatures (400–550 °C). At low temperatures, all Cu-containing samples display rapid NOx/NH$_3$ conversion increase with increasing temperature. The 2Cu sample displays superior NOx reduction efficiency versus the 3Cu sample, even though the 3Cu sample contains higher amount of isolated Cu^{II}-ions (Table 2). This serves as another piece evidence for the presence of external surface CuO on the 3Cu sample that blocks interactions between SCR reactants and isolated Cu^{II}-ions. The 2Cu sample also displays somewhat superior NOx reduction efficiency versus the 2Cu1Pd sample; such activity difference serves as evidence for Pd poisoning. As shown in Table 2, the 2Cu sample contains more isolated Cu^{II}-ions than 2Cu1Pd, further suggesting that the poisoning effect is due to Pd-ions destabilizing $ZCu^{II}OH$. In contrast, the 3Cu and 3Cu1Pd samples display highly similar NOx reduction efficiency in this temperature regime. Both samples perform slightly inferior to 2Cu1Pd. Overall, the Pd poisoning effect within this temperature regime is rather weak and not consistently observed, obviously complicated by the presence of external surface CuO. The 1 Pd sample does not display any SCR activity below 200 °C.

At intermediate temperatures, NH$_3$ conversions over all Cu-containing samples reach ~100%, i.e., SCR is now mass-transfer limited. As such, data obtained within this temperature window are not suitable for evaluating possible Pd poisoning effects. However, it is
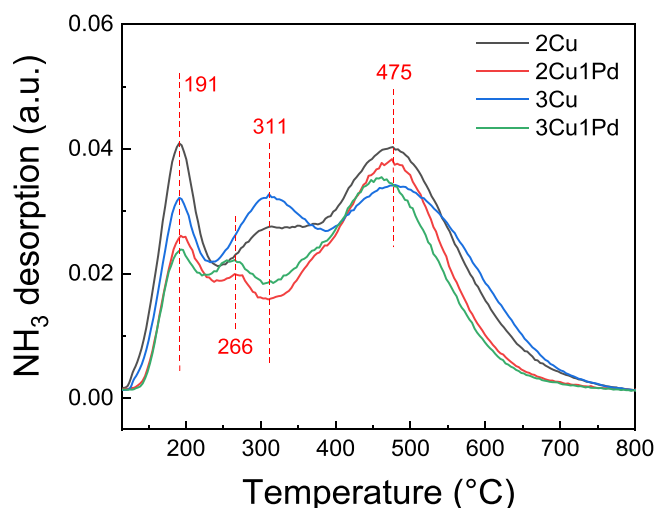

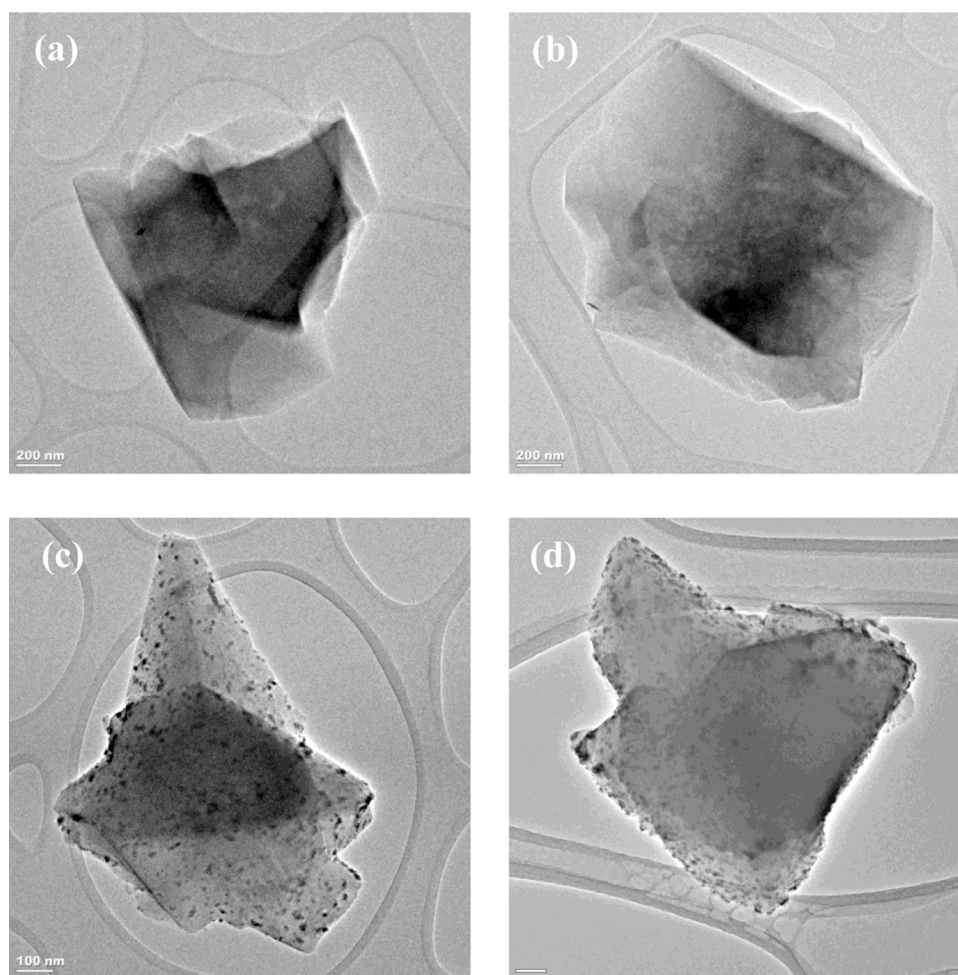**Fig. 4.** NH$_3$-TPD profiles for the fresh Cu/SSZ-13 and Pd-Cu/SSZ-13 samples.

Fig. 5. TEM images for the fresh Cu/SSZ-13 and Cu-Pd/SSZ-13 catalysts: (a) 2Cu (b) 3Cu (c) 2Cu1Pd and (d) 3Cu1Pd.

important to note that the 1 Pd sample becomes active in catalyzing NH$_3$ oxidation above ~300 °C. This is important for understanding the direct impact of Pd and interaction of Pd and CuO at higher temperatures.

At high temperatures, NOx conversion over the 2Cu sample declines only moderately with increasing temperature and remains above 80% at 550 °C. In contrast, NOx conversion quickly decreases with increasing temperature over the 2Cu1Pd sample, reaching ~32% at 550 °C. Therefore, a clear Pd poisoning effect exists for 2Cu1Pd at such high temperatures. Interestingly, NO conversions over 3Cu1Pd at such high temperatures are even slightly higher than 3Cu, that is, Pd poisoning is not observed on 3Cu1Pd.

Since both 2Cu1Pd and 3Cu1Pd reach 100% NH$_3$ conversions above 400 °C where the marked difference is observed between the two catalysts, such reduction in NOx efficiency can be readily attributed to non-selective NH$_3$ oxidation. Note from Fig. 6b that the 1 Pd sample becomes highly active in NH$_3$ oxidation above 400 °C. Therefore, it is evident that the Pd in 2Cu1Pd is more active than the Pd in 3Cu1Pd in catalyzing NH$_3$ oxidation above ~400 °C, causing 2Cu1Pd to lose more high-temperature SCR selectivity. Herein, we propose our central hypothesis of the study, i.e., PdO deposited on 3Cu1Pd interacts with external surface CuO to form mixed oxide solid solution, which displays lower oxidizing capacity than pure PdO deposited on 2Cu1Pd. Note that our catalyst textural property analysis (Table 1) indicates clear connectivity between PdO and external surface CuO on 3Cu1Pd. Note also that in previous studies, similar CuO-PdO solid solution has been reported to form on multiple supports, such as CeO$_2$ and SiO$_2$, which exhibits altered catalytic activity as compared to the single oxide components [44–47]. In the following, we provide additional evidence to support

this hypothesis by studying (i) a physical mixture of Cu & Pd, and (ii) NH$_3$ oxidation behavior of the catalysts.

Fig. 7 displays NOx and NH$_3$ conversions versus temperature on a physical mixture of 2Cu and 1 Pd samples (denoted 2Cu1Pd-PM). This sample was prepared by mixing equal weights of the 1 Pd and 2Cu samples via grinding followed by calcination at 550 °C for 4 h in static air. In comparison to the 2Cu sample (Fig. 6), this physical mixture shows clear high-temperature SCR selectivity decreases. PdO is not volatile and thus not anticipated to migrate from the "1 Pd" portion to the "2Cu" portion of the mixture during calcination and SCR reaction. Therefore, the decrease in high-temperature SCR shown in Fig. 7 is clearly attributed to non-selective NH$_3$ oxidation on PdO and demonstrates that PdO can indeed lower SCR performance at high-temperature on 2Cu1Pd and 3Cu1Pd.

Fig. 8a shows the results of NH$_3$ oxidation testing in the samples. The onset of the NH$_3$ oxidation is ~200 °C for the Cu-containing samples and ~250 °C for 1 Pd, and all samples show ~100% conversion above 450 °C. For the 2Cu sample, NH$_3$ conversion increases rapidly from ~200 °C to ~300 °C, and then maintains relatively unchanged in the 300–350 °C temperature window. This unique kinetic behavior is also found in standard SCR [18,48]; it is caused by an active site transition effect, that is, a transition from NH$_3$-solvated mobile Cu active sites to immobilized Cu as temperature rises. As such, NH$_3$ oxidation below 350 °C is largely sustained on mobile Cu-ions in this catalyst. It is interesting to note that the 2Cu1Pd catalyst is inferior to 2Cu below 400 °C, again suggesting a Pd poisoning effect attributed to Pd destabilizing ZCu^{II}OH (Table 2). 3Cu is more active than 2Cu below ~400 °C despite similar amounts of isolated Cu-ions. This clearly indicates that
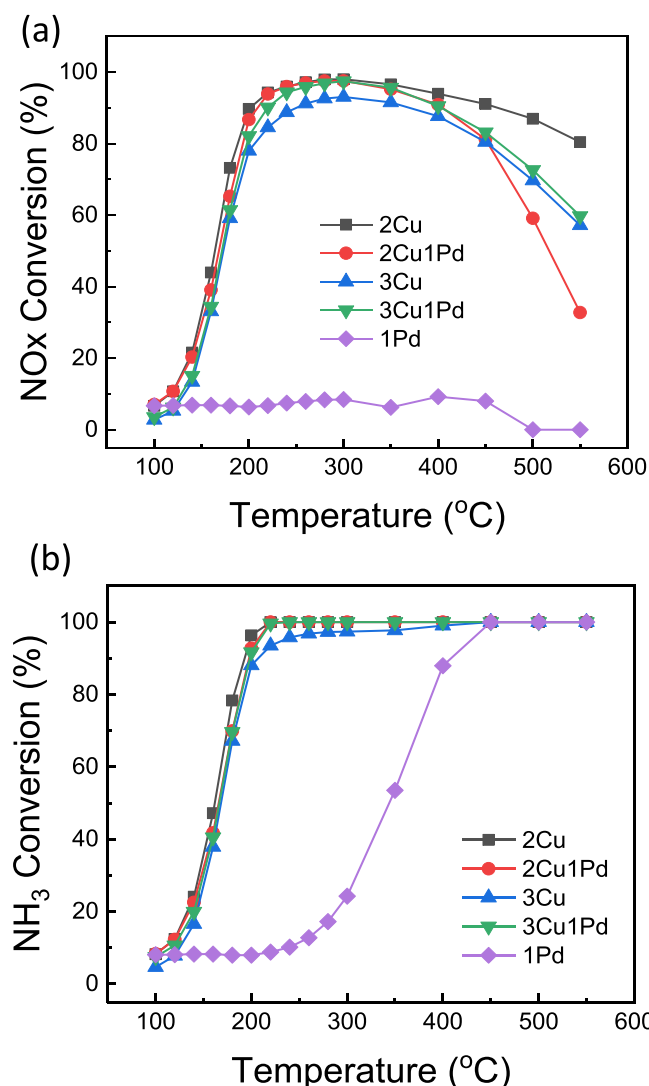
Fig. 6. NOx conversion (a) and NH$_3$ conversion (b) as a function of temperature in standard SCR on fresh 2Cu, 2Cu1Pd, 3Cu, 3Cu1Pd and 1 Pd catalysts. Reactant feed contains 350 ppm of NOx (NO + ~10 ppm NO$_2$), 350 ppm of NH$_3$, 14% O$_2$, 2.5% H$_2$O balanced with N$_2$ at a GHSV of ~300,000 h^{-1}.
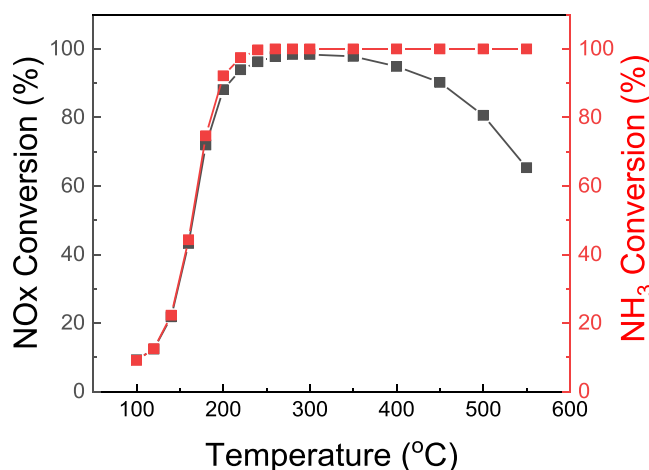

Fig. 7. NOx conversion as a function of temperature in standard SCR over the physically mixed 2Cu1Pd-PM sample. Reactant feed contains 350 ppm of NOx (NO + ~10 ppm NO$_2$), 350 ppm of NH$_3$, 14% O$_2$, 2.5% H$_2$O balanced with N$_2$ at a GHSV of ~300,000 h^{-1}.
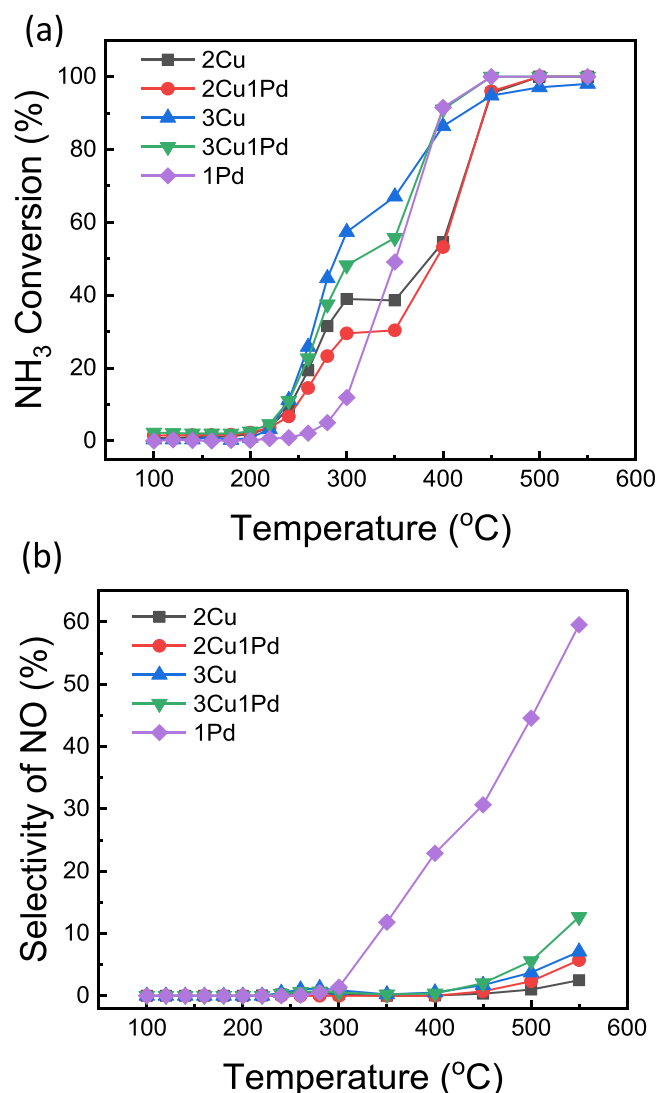

Fig. 8. NH$_3$ conversion (a) and NO selectivity (b) as a function of temperature in NH$_3$ oxidation reaction on fresh 2Cu, 2Cu1Pd, 3Cu, 3Cu1Pd and 1 Pd catalysts. Reactant feed contains 380 ppm of NH$_3$, 14% O$_2$, 2.5% H$_2$O balanced with N$_2$ at a GHSV of ~300,000 h^{-1}.

the CuO clusters in 3Cu contribute to low-temperature NH$_3$ oxidation. In comparing catalytic activity between the 3Cu and 3Cu1Pd samples, an apparent Pd poisoning effect is also found below 400 °C. However, the nature of this effect is likely more complex than 2Cu1Pd. Analogous to 2Cu1Pd, Pd deposition on 3Cu1Pd lowers isolated Cu^{II}-ion content (which is anticipated to lower low-temperature NH$_3$ oxidation activity), but PdO-CuO interactions in 3Cu1Pd also lower the NH$_3$ oxidation activity of CuO clusters. To further verify this argument, we prepared γ-Al$_2$O$_3$ (Sasol CATALOX SBa-200) supported 2Cu, 2Cu1Pd and 1 Pd model catalysts and carried out NH$_3$ oxidation tests. Unlike SSZ-13, γ-Al$_2$O$_3$ does not have ion exchange capacity so that PdO-CuO solid solution formation is facilitated. From the results detailed in Fig. S3, NH$_3$ oxidation activity and selectivity to NOx are indeed substantially lower on 2Cu1Pd-Al$_2$O$_3$ than on 1 Pd-Al$_2$O$_3$.

As a side note, in applying NH$_3$ oxidation to elucidate Pd poisoning effect, we observed an interesting NH$_3$ affinity effect. Note that at 350 and 400 °C, 1 Pd displays substantially higher activity than 2Cu1Pd. This can be understood by invoking preferred NH$_3$ chemisorption on Cu sites, i.e., when Cu-ions and PdO coexist, NH$_3$ prefers to adsorb and react on the otherwise less active Cu sites. This notion is corroborated by the side product NO formation data shown in Fig. 8b. In comparison to the

1 Pd sample, both 2Cu1Pd and 3Cu1Pd samples display much lower NO selectivity.

To summarize, our SCR and NH$_3$ oxidation reaction results are consistent with two Pd poisoning mechanisms. At temperatures < 300 °C where PdO has negligible to low NH$_3$ oxidation activity, the main impact of Pd is the displacement of isolated Cu^{II}-ions and in particular ZCu^{II}OH. This is caused by Pd-ions that diffuse into the chabazite bulk, and the impact is loss of isolated Cu^{II}-ions that deteriorates low-temperature SCR (and NH$_3$ oxidation). At temperatures > 350 °C where PdO becomes active for NH$_3$ oxidation, Pd acts as a poison greatly deteriorating SCR selectivity. However, the strong oxidizing capacity of PdO is mitigated in the presence of CuO by forming CuO-PdO solid solutions with much lower oxidizing capacity. However, since CuO itself is also detrimental to high-temperature SCR, it is more desirable to use other oxides that can "trap" PdO but do not catalyze SCR side reactions. Note that in our previous study, ZrO$_2$ was added to Cu/SSZ-13 to eliminate detrimental CuO clusters via formation of ZrO$_2$-CuO solid solutions [49]. In this regard, it is possible to mitigate Pd poisoning (or more generally, PGM poisoning) of Cu-zeolite SCR catalysts by applying metal oxide cocatalysts (e.g., ZrO$_2$) that can "trap" both PGM and CuO. This strategy is currently being investigated in our laboratories.

We also note that for both SCR catalysts and Cu/zeolite components of ammonia slip catalysts, it is unlikely that PGM contamination level will ever reach as high as ~1 wt% during practical applications. However, the amount of PGM likely only influences the severity, but not the mechanisms of poisoning. As such, Pd poisoning mechanisms derived here should be considered practically relevant.

3.2.2. Hydrothermally aged (HTA) catalysts

To elucidate the effects of Pd on hydrothermal stability of Cu/SSZ-13, fresh Cu/SSZ-13 and Pd-Cu/SSZ-13 samples were treated hydrothermally at 800 °C for 24 h under a flow of air containing 10% water vapor. Following this treatment, their catalytic performance was tested using both standard SCR and NH$_3$ oxidation reactions. Fig. 9 shows standard SCR NOx and NH$_3$ conversion versus temperature plots. At temperatures < 350 °C, all samples show similar NOx and NH$_3$ conversions at the same temperature. This result is anticipated: as our catalyst textural property characterizations (Table 1, Fig. 1) and isolated Cu^{II}-ion content measurement (Table 2) demonstrate, the presence of Pd does not aggravate such merits during hydrothermal aging. Particularly, all aged catalysts contain similar amount of SCR active Cu^{II}-ion sites. In the high temperature regime, interestingly, Pd displays opposing effects to SCR selectivity, i.e., 2Cu1Pd-HTA shows inferior SCR selectivity as compared to 2Cu-HTA, whereas 3Cu1Pd-HTA shows superior SCR selectivity as compared to 3Cu-HTA. This behavior is likely the combination of both CuO and Pd, as explained below.

Harsh hydrothermal aging (at 700 °C and above) of Cu/SSZ-13 commonly causes framework dealumination and agglomeration of isolated Cu^{II}-ions (especially ZCu^{II}OH) to CuO clusters, leading to decreased NOx reduction efficiency, i.e., activity loss at low temperatures and selectivity loss at high temperatures. This notion is evidenced by comparing light-off curves of the fresh 2Cu sample shown in Fig. 6a and the 2Cu-HTA sample shown in Fig. 9a. We have shown above that adding Pd to fresh 2Cu causes isolated Cu^{II}-ion content to drop from 1.92% for 2Cu to 1.67% for 2Cu1Pd (Table 2), caused by displacement of ZCu^{II}OH species by Pd^{II}-ions. It is interesting that hydrothermal aging of 2Cu1Pd barely leads to additional decrease of isolated Cu^{II}-ion content (2Cu1Pd-HTA contains 1.60% isolated Cu^{II}-ions). This suggests that external surface PdO and Z$_2$Cu^{II} species are thermodynamically the most stable Pd and Cu moieties, respectively, under hydrothermal aging conditions, i.e., external surface PdO does not convert to isolated Pd^{II}-ions during aging and further catastrophically deteriorate the low-temperature SCR function by displacing Cu^{II}-ions. Still, since both CuO clusters and PdO catalyze non-selective NH$_3$ oxidation, high-temperature SCR selectivity for 2Cu1Pd-HTA is still inferior to 2Cu-HTA. However, likely due to more thorough CuO-PdO intermixing
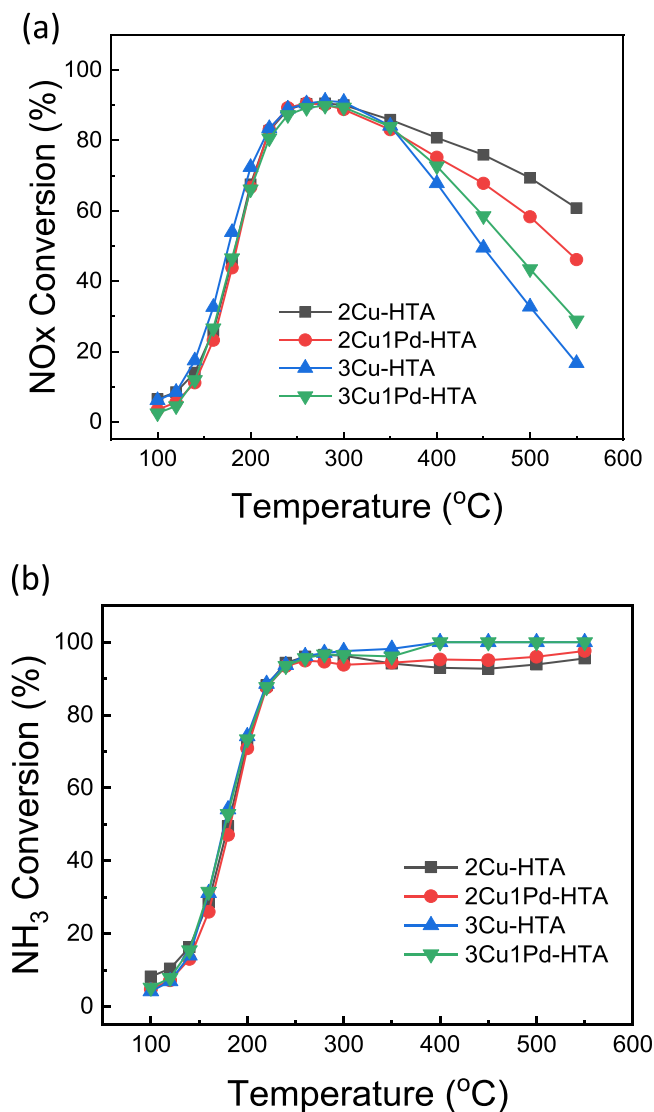

Fig. 9. NOx conversion (a) and NH$_3$ conversion (b) as a function of temperature in standard SCR on hydrothermally aged 2Cu, 2Cu1Pd, 3Cu and 3Cu1Pd catalysts. Reactant feed contains 350 ppm of NOx (NO + ~10 ppm NO$_2$), 350 ppm of NH$_3$, 14% O$_2$, 2.5% H$_2$O balanced with N$_2$ at a GHSV of ~300,000 h^{-1}.

during aging, high-temperature SCR selectivity for 3Cu1Pd-HTA is superior to 3Cu-HTA. This intermixing also appears to benefit the maintenance of isolated Cu^{II}-ions. As Table 2 shows, 3Cu1Pd-HTA contains slightly more isolated Cu^{II}-ions than 3Cu-HTA. Note that the similar phenomenon was found previously on a Pt poisoned Cu/SAPO-34 SCR catalyst [12].

Finally, Fig. 10a shows the NH$_3$ oxidation light-off curves over the hydrothermally aged catalysts, and Fig. 10b displays formation of the side product NO. These data are fully in line with SCR results shown in Fig. 9, i.e., The activity order shown here, i.e., 3Cu-HTA > 3Cu1Pd-HTA > 2Cu1Pd-HTA > 2Cu-HTA, is fully consistent with the inverse high-temperature SCR selectivity order shown in Fig. 9a. As such, these data will not be discussed any further. We emphasize again that the data shown in Fig. 10 reinforce the concept of using oxide additives to "trap" detrimental species (or poisons) via solid solution formation [49].

4. Conclusions

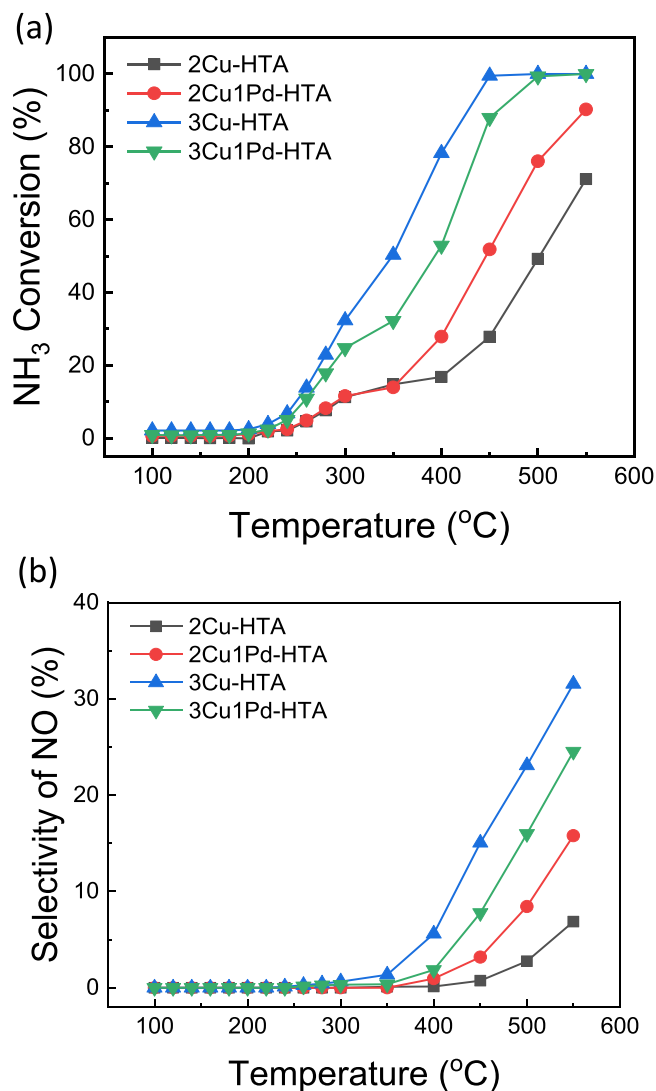In the present study, effects of Pd poisoning to Cu/SSZ-13 SCR

Fig. 10. NH$_3$ conversion (a) and NO selectivity (b) as a function of temperature in NH$_3$ oxidation on hydrothermally aged 2Cu, 2Cu1Pd, 3Cu and 3Cu1Pd catalysts. Reactant feed contains 380 ppm of NH$_3$, 14% O$_2$, 2.5% H$_2$O balanced with N$_2$ at a GHSV of ~300,000 h^{-1}.

catalysts are investigated. Based on catalyst characterizations using EPR, TEM, temperature-programmed chemical titrations, etc., and standard SCR and NH$_3$ oxidation kinetic measurements, two poisoning mechanisms are identified: (1) Pd diffuses into zeolite pores in the form of Pd^{II}-ions and displaces SCR active, ZCu^{II}OH species. (2) Pd deposits on zeolite external surface in the form of PdO. The first mechanism deteriorates a Cu/SSZ-13 catalyst by lowering active site density and by the conversion of ZCu^{II}OH to unwanted CuO clusters. The second mechanism deteriorates a Cu/SSZ-13 catalyst by lowering high-temperature SCR selectivity. Up to a Pd loading of ~1 wt% studied here, both effects are rather minor and do not lead to catastrophic poisoning. For Cu/SSZ-13 containing external surface CuO, the detrimental effect of PdO becomes alleviated via formation of CuO-PdO solid solution, which displays lower oxidizing capacity than PdO. This latter finding suggests that PGM poisoning can be managed by applying oxide additives (e.g., ZrO$_2$) that effectively trap PGM poisons.

CRediT authorship contribution statement

Yiqing Wu: Catalyst preparation, Data collection and processing (reaction test, characterization), Writing – original draft. **Yilin Wang:**

Catalyst preparation, Data collection and processing (reaction test, characterization), Writing – original draft. **Eric D. Walter:** Data collection and processing (EPR characterization). Discussion. **Kenneth G. Rappé:** Supervision, Conceptualization, Discussion, Writing – review & editing. **Yong Wang:** Supervision, Conceptualization, Discussion, Writing – review & editing. **Feng Gao:** Supervision, Conceptualization, Discussion, Writing – review & editing.

Declaration of Competing Interest

The authors declare that they have no known competing financial interests or personal relationships that could have appeared to influence the work reported in this paper.

Data availability

Data will be made available on request.

Appendix A. Supporting information

Supplementary data associated with this article can be found in the online version at doi:10.1016/j.apcatb.2023.122673.

References

[1] F. Gao, C.H.F. Peden, Recent progress in atomic-level understanding of Cu/SSZ-13 selective catalytic reduction catalysts, Catalysts 8 (2018) 140.

[2] E. Borfecchia, P. Beato, S. Svelle, U. Olsbye, C. Lamberti, S. Bordiga, Cu-CHA – a model system for applied selective redox catalysis, Chem. Soc. Rev. 47 (2018) 8097–8133.

[3] A.M. Beale, F. Gao, I. Lezcano-Gonzalez, C.H.F. Peden, J. Szanyi, Recent advances in automotive catalysis for NOx emission control by small-pore microporous materials, Chem. Soc. Rev. 44 (2015) 7371–7405.

[4] Y. Gu, W.S. Epling, Passive NOx adsorber: an overview of catalyst performance and reaction chemistry, Appl. Catal. A Gen. 570 (2019) 1–14.

[5] Y. Zheng, L. Kovarik, M.H. Engelhard, Y. Wang, F. Gao, J. Szanyi, Low-temperature Pd/Zeolite passive NOx adsorbers: structure, performance, and adsorption chemistry, J. Phys. Chem. C 121 (2017) 15793–15803.

[6] K. Khivantsev, X. Wei, L. Kovarik, N.R. Jaegers, E.D. Walter, P. Tran, Y. Wang, J. Szanyi, Pd/FER vs Pd/SSZ-13 passive NOx adsorbers: adsorbate-controlled location of atomically dispersed Pd(II) in FER determines high activity and stability, Angew. Chem. Int. Ed., n/a.

[7] K. Leistner, C. Gonzalez Braga, A. Kumar, K. Kamasamudram, L. Olsson, Volatilisation and subsequent deposition of platinum oxides from diesel oxidation catalysts, Appl. Catal. B Environ. 241 (2019) 338–350.

[8] R.S. Ghosh, T.T. Le, T. Terlier, J.D. Rimer, M.P. Harold, D. Wang, Enhanced selective oxidation of ammonia in a Pt/Al2O3@Cu/ZSM-5 core–shell catalyst, ACS Catal. 10 (2020) 3604–3617.

[9] T. Zhang, H. Chang, C. You, C. Shi, J. Li, Excellent activity and selectivity of one-pot synthesized Cu–SSZ-13 catalyst in the selective catalytic oxidation of ammonia to nitrogen, Environ. Sci. Technol. 52 (2018) 4802–4808.

[10] S. Shrestha, M.P. Harold, K. Kamasamudram, A. Kumar, L. Olsson, K. Leistner, Selective oxidation of ammonia to nitrogen on bi-functional Cu–SSZ-13 and Pt/Al2O3 monolith catalyst, Catal. Today 267 (2016) 130–144.

[11] I. Lezcano-Gonzalez, U. Deka, H.E. van der Bij, P. Paalanen, B. Arstad, B. M. Weckhuysen, A.M. Beale, Chemical deactivation of Cu-SSZ-13 ammonia selective catalytic reduction (NH3-SCR) systems, Appl. Catal. B Environ. 154–155 (2014) 339–349.

[12] T. Yu, M. Xu, Y. Huang, J. Wang, J. Wang, L. Lv, G. Qi, W. Li, M. Shen, Insight of platinum poisoning Cu/SAPO-34 during NH3-SCR and its promotion on catalysts regeneration after hydrothermal treatment, Appl. Catal. B Environ. 204 (2017) 525–536.

[13] Y.R. Cui, Y.L. Wang, D.H. Mei, E.D. Walter, N.M. Washton, J.D. Holladay, Y. Wang, J. Szanyi, C.H.F. Peden, F. Gao, Revisiting effects of alkali metal and alkaline earth

co-cation additives to Cu/SSZ-13 selective catalytic reduction catalysts, J. Catal. 378 (2019) 363–375.

[14] A.J. Shih, J.M. González, I. Khurana, L.P. Ramírez, A. Peña L, A. Kumar, A.L. Villa, Influence of ZCuOH, Z2Cu, and extraframework CuxOy species in Cu-SSZ-13 on N2O formation during the selective catalytic reduction of NOx with NH3, ACS Catal. 11 (2021) 10362–10376.

[15] Y. Cui, J. Zhu Chen, B. Peng, L. Kovarik, A. Devaraj, Z. Li, T. Ma, Y. Wang, J. Szanyi, J.T. Miller, Y. Wang, F. Gao, Onset of high methane combustion rates over supported palladium catalysts: from isolated Pd cations to PdO nanoparticles, JACS Au 1 (2021) 396–408.

[16] Z. Chen, M. Wang, J. Wang, C. Wang, J. Wang, W. Li, M. Shen, Investigation of crystal size effect on the NOx storage performance of Pd/SSZ-13 passive NOx adsorbers, Appl. Catal. B Environ. 291 (2021).

[17] Y. Zhang, Y. Wu, Y. Peng, J. Li, E.D. Walter, Y. Chen, N.M. Washton, J. Szanyi, Y. Wang, F. Gao, Quantitative Cu counting methodologies for Cu/SSZ-13 selective catalytic reduction catalysts by electron paramagnetic resonance spectroscopy, J. Phys. Chem. C 124 (2020) 28061–28073.

[18] F. Gao, D.H. Mei, Y.L. Wang, J. Szanyi, C.H.F. Peden, Selective catalytic reduction over Cu/SSZ-13: linking homo- and heterogeneous catalysis, J. Am. Chem. Soc. 139 (2017) 4935–4942.

[19] C. Paolucci, A.A. Parekh, I. Khurana, J.R. Di Iorio, H. Li, J.D.A. Caballero, A. J. Shih, T. Anggara, W.N. Delgass, J.T. Miller, F.H. Ribeiro, R. Gounder, W. F. Schneider, Catalysis in a cage: condition-dependent speciation and dynamics of exchanged Cu cations in SSZ-13 zeolites, J. Am. Chem. Soc. 138 (2016) 6028–6048.

[20] C. Negri, T. Selleri, E. Borfecchia, A. Martini, K.A. Lomachenko, T.V.W. Janssens, M. Cutini, S. Bordiga, G. Berlier, Structure and reactivity of oxygen-bridged diamino dicopper(II) complexes in Cu-ion-exchanged chabazite catalyst for NH3-mediated selective catalytic reduction, J. Am. Chem. Soc. 142 (2020) 15884–15896.

[21] S. Han, Q. Ye, S. Cheng, T. Kang, H. Dai, Effect of the hydrothermal aging temperature and Cu/Al ratio on the hydrothermal stability of CuSSZ-13 catalysts for NH3-SCR, Catal. Sci. Technol. 7 (2017) 703–717.

[22] Y.J. Kim, J.K. Lee, K.M. Min, S.B. Hong, I.-S. Nam, B.K. Cho, Hydrothermal stability of CuSSZ13 for reducing NOx by NH3, J. Catal. 311 (2014) 447–457.

[23] F. Gao, Y. Wang, N.M. Washton, M. Kollár, J. Szanyi, C.H.F. Peden, Effects of alkali and alkaline earth cocations on the activity and hydrothermal stability of Cu/SSZ-13 NH3–SCR catalysts, ACS Catal. 5 (2015) 6780–6791.

[24] F. Gao, N.M. Washton, Y. Wang, M. Kollár, J. Szanyi, C.H.F. Peden, Effects of Si/Al ratio on Cu/SSZ-13 NH3-SCR catalysts: implications for the active Cu species and the roles of Brønsted acidity, J. Catal. 331 (2015) 25–38.

[25] J. Hun Kwak, H. Zhu, J.H. Lee, C.H.F. Peden, J. Szanyi, Two different cationic positions in Cu-SSZ-13? Chem. Commun. 48 (2012) 4758–4760.

[26] Y. Shan, W. Shan, X. Shi, J. Du, Y. Yu, H. He, A comparative study of the activity and hydrothermal stability of Al-rich Cu-SSZ-39 and Cu-SSZ-13, Appl. Catal. B Environ. 264 (2020), 118511.

[27] S. Zhou, F. Tang, H. Wang, S. Wang, L. Liu, Effect of Cu concentration on the selective catalytic reduction of NO with ammonia over aluminosilicate zeolite SSZ-13 catalysts, J. Phys. Chem. C 125 (2021) 14675–14680.

[28] M.-F. Luo, Z.-Y. Hou, X.-X. Yuan, X.-M. Zheng, Characterization study of CeO2 supported Pd catalyst for low-temperature carbon monoxide oxidation, Catal. Lett. 50 (1998) 205–209.

[29] W.C. Conner, J.L. Falconer, Spillover in heterogeneous catalysis, Chem. Rev. 95 (1995) 759–788.

[30] B.D. Adams, A. Chen, The role of palladium in a hydrogen economy, Mater. Today 14 (2011) 282–289.

[31] Y. Zhang, Y. Peng, J. Li, K. Groden, J.-S. McEwen, E.D. Walter, Y. Chen, Y. Wang, F. Gao, Probing active-site relocation in Cu/SSZ-13 SCR catalysts during hydrothermal aging by in situ EPR spectroscopy, kinetics studies, and DFT calculations, ACS Catal. 10 (2020) 9410–9419.

[32] J. Song, Y. Wang, E.D. Walter, N.M. Washton, D. Mei, L. Kovarik, M.H. Engelhard, S. Prodinger, Y. Wang, C.H.F. Peden, F. Gao, Toward rational design of Cu/SSZ-13

[33] A. Godiksen, F.N. Stappen, P.N.R. Vennestrøm, F. Giordanino, S.B. Rasmussen, L. F. Lundegaard, S. Mossin, Coordination environment of copper sites in Cu-CHA zeolite investigated by electron paramagnetic resonance, J. Phys. Chem. C 118 (2014) 23126–23138.

[34] V.L. Sushkevich, A.V. Smirnov, J.A. van Bokhoven, Autoreduction of copper in zeolites: role of topology, Si/Al ratio, and copper loading, J. Phys. Chem. C 123 (2019) 9926–9934.

[35] Y.N. Zhang, J. Zhang, H.L. Wang, W.N. Yang, C.Z. Wang, Y. Peng, J.J. Chen, J. H. Li, F. Gao, Selective catalytic reduction of NOx with NH3 over Cu/SSZ-13: elucidating dynamics of Cu active sites with in situ UV-Vis spectroscopy and DFT calculations, J. Phys. Chem. C 126 (2022) 8720–8733.

[36] P.C. Bruzzese, E. Salvadori, B. Civalleri, S. Jaeger, M. Hartmann, A. Poeppl, M. Chiesa, The structure of monomeric hydroxo-C-II species in Cu-CHA. A quantitative assessment, J. Am. Chem. Soc. (2022).

[37] J. Song, Y.L. Wang, E.D. Walter, N.M. Washton, D.H. Mei, L. Kovarik, M. H. Engelhard, S. Prodinger, Y. Wang, C.H.F. Peden, F. Gao, Toward rational design of Cu/SSZ-13 selective catalytic reduction catalysts: implications from atomic-level understanding of hydrothermal stability, ACS Catal. 7 (2017) 8214–8227.

[38] F. Gao, J. Szanyi, On the hydrothermal stability of Cu/SSZ-13 SCR catalysts, Appl. Catal. A Gen. 560 (2018) 185–194.

[39] Y.N. Zhang, Y. Peng, J.H. Li, K. Groden, J.S. Mcewen, E.D. Walter, Y. Chen, Y. Wang, F. Gao, Probing active-site relocation in Cu/SSZ-13 SCR catalysts during hydrothermal aging by In Situ EPR spectroscopy, kinetics studies, and DFT calculations, ACSCatal. 10 (2020) 9410–9419.

[40] Y. Wu, Y. Ma, Y. Wang, K.G. Rappé, N.M. Washton, Y. Wang, E.D. Walter, F. Gao, Rate controlling in low-temperature standard NH3-SCR: implications from operando EPR spectroscopy and reaction kinetics, J. Am. Chem. Soc. 144 (2022) 9734–9746.

[41] K. Khivantsev, N.R. Jaegers, I.Z. Koleva, H.A. Aleksandrov, L. Kovarik, M. Engelhard, F. Gao, Y. Wang, G.N. Vayssilov, J. Szanyi, Stabilization of super electrophilic Pd+2 cations in small-pore SSZ-13 zeolite, J. Phys. Chem. C 124 (2020) 309–321.

[42] R.Q. Zhang, J.S. McEwen, M. Kollar, F. Gao, Y.L. Wang, J. Szanyi, C.H.F. Peden, NO chemisorption on Cu/SSZ-13: a comparative study from infrared spectroscopy and DFT calculations, ACS Catal. 4 (2014) 4093–4105.

[43] F. Gao, E.D. Walter, N.M. Washton, J. Szanyi, C.H.F. Peden, Synthesis and evaluation of Cu/SAPO-34 catalysts for NH3-SCR 2: solid-state ion exchange and one-pot synthesis, Appl. Catal. B Environ. 162 (2015) 501–514.

[44] G.L. Christensen, M.A. Langell, Characterization of copper palladium oxide solid solutions by X-ray diffraction, X-ray photoelectron spectroscopy, and auger electron spectroscopy, J. Phys. Chem. C 117 (2013) 7039–7049.

[45] M. Kang, M.W. Song, K.L. Kim, SMSI effect on ceria supported Cu-Pd catalysts in the hydrogenation of 1,3-butadiene, React. Kinet. Catal. Lett. 75 (2002) 177–183.

[46] E. Torralba, N. Blanchard, C. Cachet-Vivier, D. Muller-Bouvet, J. González, S. Bastide, Electrochemical study of carbon dioxide reduction at copper–palladium nanoparticles: influence of the bimetallic composition in the CO poisoning tolerance, Electrochim. Acta 354 (2020), 136739.

[47] X. Jiang, N. Koizumi, X. Guo, C. Song, Bimetallic Pd–Cu catalysts for selective CO2 hydrogenation to methanol, Appl. Catal. B Environ. 170–171 (2015) 173–185.

[48] C. Paolucci, I. Khurana, A.A. Parekh, S. Li, A.J. Shih, H. Li, J.R. Di Iorio, J. D. Albarracin-Caballero, A. Yezerets, J.T. Miller, W.N. Delgass, F.H. Ribeiro, W. F. Schneider, R. Gounder, Dynamic multinuclear sites formed by mobilized copper ions in NOx selective catalytic reduction, Science 357 (2017) 898–903.

[49] B. Peng, K.G. Rappé, Y. Cui, F. Gao, J. Szanyi, M.J. Olszta, E.D. Walter, Y. Wang, J. D. Holladay, R.A. Goffe, Enhancement of high-temperature selectivity on Cu-SSZ-13 towards NH3-SCR reaction from highly dispersed ZrO2, Appl. Catal. B Environ. 263 (2020), 118359.